Journal of
Materials Chemistry A

ROYAL SOCIETY
OF CHEMISTRY

PAPER

View Article Online
View Journal | View Issue

Cite this: *J. Mater. Chem. A*, 2026, **14**, 14381

A low temperature solution-chemical process for fluoride salt (NaF) waste immobilization into metal halide perovskite structured Na_2SnF_6

Saurabh Kumar Sharma, [a] Dong Zhao,[a] Weiguang Zhu,[a] Kun Yang,[a]
Mingyang Zhao[a] and Jie Lian *[ab]

Received 1st January 2026
Accepted 5th February 2026

DOI: 10.1039/d6ta00002a

rsc.li/materials-a

Complex salt waste streams generated from chemical reprocessing of spent nuclear fuels and advanced molten salt reactor technologies require innovative materials and processes for effective immobilization and management. In this study, we report a simple, low-temperature, solution-based approach for immobilizing fluoride salts, specifically alkali halides, into metal halide perovskite (MHP) waste forms. Using NaF as a representative system, systematic experiments were conducted to immobilize alkali-halides into Na_2SnF_6, achieving a high fluorine content of 40.9 wt% and a fluoride loading capacity of 57.4 wt%. By tailoring key parameters such as the use of surfactants, salt grain size, and reaction temperature, the low temperature solution chemistry process achieves consistently high immobilization efficiencies above 95%. X-Ray diffraction (XRD) analysis coupled with Rietveld refinement confirmed that Na_2SnF_6 predominantly crystallizes in the tetragonal $P4_2/mnm$ structure as the primary phase. A hexagonal metastable phase was also observed, attributed to rapid precipitation during synthesis. Microstructural characterization using scanning electron microscopy (SEM) and energy-dispersive X-ray spectroscopy (EDS) confirms uniform elemental distribution and microchemical compositions consistent with the Na_2SnF_6 crystal structure. Thermogravimetric analysis (TGA) demonstrates thermal stability of the synthesized waste forms up to 400 °C. This work establishes a foundational, cost-effective pathway for immobilizing alkali fluoride salt waste into MHP-type structures with high waste loading using novel low-temperature solution chemistry for effective management of salt waste.

1. Introduction

Molten salt reactors (MSRs) have gained considerable interest as Generation IV reactors in which molten salts, such as fluorides or chlorides, are used as either heat carriers or both coolant and fuel carriers in reactors.[1] Fluoride- and chloride-based MSRs generate complex salt waste streams that require immobilization for long-term storage. Molten salt waste is known for strong corrosivity, poor chemical durability, low melting temperature, highly volatile and a highly hygroscopic nature. Therefore, it is essential to effectively immobilize salt waste into a chemically durable waste form with high waste loading. Similarly, the reprocessing of spent nuclear fuels also generates salt waste, highlighting the need for their effective immobilization strategies to ensure safe disposal.

Direct immobilization of unseparated salts is not an attractive option for salt management due to the lack of recovery of expensive elements like ^{7}Li and ^{37}Cl. However, the high volatility associated with the alkalis and halides, and their low solubility poses a significant challenge for immobilization of alkali-halides in borosilicate glass, which is commonly used for vitrifying high level radioactive waste.[2,3] It is not feasible to immobilize the salt waste into a single waste form with high waste loading levels. Separating salt waste is highly desirable to enable more efficient waste management and to facilitate the design of multiple waste forms that optimize chemical durability and enhance waste loading. Various ceramic waste forms namely, apatite, phosphate, sodalite, nesosilicate, cancrinite, and pyrochlore have been studied for immobilization of salt waste constituents.[4–7] The selection of waste forms for immobilizing salt-based nuclear waste has expanded beyond glasses and ceramics to include composites like glass-bonded and metal-bonded ceramics.[8–10]

There are a few reports on immobilization of fluoride waste into phosphate glass due to lower processing temperature and higher halide solubility as compared to borosilicate glass. Sun *et al.* developed a sodium aluminophosphate (NaAlP) glassy waste form to immobilize 20 mol% of MF_n (where M = Cs, Sr, Zr, Ce, and Sm) and further addition of iron oxide to increase the chemical durability, resulting in low waste loading (6.4 mol%).[11] Liu *et al.* reported that 30 wt% SrF_2 or 10 wt% CeF_3 was

---

[a] Department of Mechanical, Aerospace, and Nuclear Engineering, Rensselaer Polytechnic Institute (RPI), New York, USA. E-mail: lianj@rpi.edu

[b] Department of Materials Science & Engineering, Rensselaer Polytechnic Institute (RPI), New York, USA

immobilized in a glassy iron phosphate waste form by vitrification at 1050–1200 °C.[12,13] They further pushed the investigation by immobilizing 22 wt% of CeF_3 in a phosphate glass matrix composed of 26 wt% Fe_2O_3–64 wt% P_2O_5–10 wt% B_2O_3 without any precipitation.[14] Jena *et al.* utilized borosilicate glass to immobilize Sr-chlorapatite up to 10–13 wt% loading without phase segregation.[15] However, detailed information regarding fluorine retention within the vitrified glass was not provided. Fluorozirconate glasses were also developed with ZBLAN composition (ZrF_4–BaF_2–LaF_3–AlF_3–NaF) for their optical properties, but poor chemical durability limits their application for halide waste immobilization.[16,17] Furthermore, lead tellurite glasses were developed to immobilize chloride salts such as alkali chlorides, alkaline earth chlorides, rare earth chlorides, and rare earth oxychlorides.[18–21] Riley *et al.* reported no perturbation in a glass network of 78% TeO_2–22% PbO on loading 5–17.5 wt% $SrCl_2$ or loading of chlorine up to 7.8%.[18] Due to their high halide solubility and lower processing temperatures, tellurite glasses are currently among the most effective materials for halide waste immobilization. However, the natural scarcity and high cost of TeO_2 limit their scalability for large-scale immobilization of halide-containing waste. In addition, secondary wastes, such as corrosive gases like HCl and HF, were also generated during the vitrification process, making high temperature glass melting – typically at several hundred degrees Celsius – an unacceptable process for the immobilization of salt waste.

New materials and advanced processes are required to immobilize salt waste with increased waste loading and minimized loss of highly volatile alkali and halides during waste incorporation and waste form processing. Alternative approaches have been sought, including a solid-state process[22,23] and hot isostatic pressing (HIPing).[24] Donald *et al.* employed a solid-state process to immobilize chloride waste in sodium aluminosilicate mineral, $Na_8(AlSiO_4)_6Cl_2$ and calcium phosphate, $Ca_5(PO_4)_3Cl$. Fluorapatite was developed to immobilize fluoride waste through coupled cation–anion substitutions. Similarly, Auxilia L. *et al.* studied $Ca_{10}(PO_4)_6F_2$ to immobilize fluoride containing waste.[25] Cao *et al.* employed wet chemical synthesis to immobilize radioactive iodine in the apatite-based waste form.[26] However, fluoride content in these crystalline mineral structures is relatively low, especially when compared to the higher fluoride loading of 17–21 wt% achieved in the HIP glass-ceramic composite waste form. Therefore, there is a need for advanced materials or mineral structures to immobilize alkali and alkaline earth halides with high waste loadings, while utilizing low-temperature processes to avoid the production of secondary waste.

A new concept of inorganic metal halide perovskites (MHPs) has been recently introduced to immobilize halide salt waste. MHPs are widely known for their application in the optoelectronic industry, recently emerging as promising candidates for nuclear waste forms owing to their compositional flexibility and diverse chemistry for immobilizing alkali and alkaline earth halides. Yang *et al.* reported successful immobilization of Cs and iodine in $Cs_3Bi_2I_9$.[27] Similarly, Cs and Cl were encapsulated into Cs_2SnCl_6, which has been reported to achieve high waste loadings of 44.5 wt% Cs and 35.6 wt% Cl.[28]

The perovskite-type structures, such as $CaTiO_3$, are generally represented by the formula ABX_3, in which 'A' is typically a larger monovalent cation, 'B' is a smaller divalent cation, and 'X' is a monovalent anion. The structure features two distinct cationic sites: the B-site cation is coordinated by six anions forming a BX_6 octahedron, while the A-site cation occupies the larger cuboctahedral interstices. In an ideal cubic perovskite structure, the X anions are located at face-centered positions, coordinating with the B-site cations located at the center of the cube. The A-site cation is situated at the corners of the cube and is 12-fold coordinated with surrounding anions. Considering the wide range of cation valence states, cations with higher oxidation states can also be incorporated into the perovskite lattice, leading to the formation of more complex perovskite-type compounds such as A_3BX_6, A_2BX_6, $A_3B_2X_9$, and A_4BX_6, all derived from the ABX_3 structure. This highlights the compositional versatility of MHPs, allowing for a broad selection of A- and B-site cations from across the periodic table.[29]

In this work, we report a novel low-temperature, solution-based approach to immobilize sodium fluoride (NaF) into an MHP compound, namely Na_2SnF_6. The synthesis of Na_2SnF_6 was systematically investigated as a function of key reaction parameters to elucidate their influence on the product yield, phase formation, microstructure and product stability. The chemical process offers high reaction yield, cost-effectiveness, and scalability. Moreover, the synthesized MHP (Na_2SnF_6) offers a high fluorine loading of 40.9 wt% and a fluoride loading capacity of 57.4 wt%, assuming near a 100% reaction yield. We have systematically explored the reaction conditions to maximize the reaction yield (>95%) and investigated how different synthesis conditions influence the structural, microstructural, and thermal decomposition behaviors of the fluoride waste containing MHPs. Finally, a monolithic sample of wasted loaded MHP (Na_2SnF_6) synthesized at room temperature was densified *via* an innovative cold sintering process (CSP) using spark plasma sintering (SPS). DMSO was used as an additive to enhance diffusion and particle bonding during the CSP to demonstrate the consolidation of Na_2SnF_6 MHP waste forms at 200 °C to mitigate potential loss of volatile wastes.

2. Experimental details

2.1. Synthesis

The MHP (Na_2SnF_6) was synthesized through a cost-effective solution-based chemical process at low-temperatures of less than 100 °C. Sodium fluoride (NaF) was used as a representative salt to simulate separated salt waste of alkali halide, and NaF is also a major component in the FLiNaK salt coolant. In addition to NaF, tin(IV) chloride pentahydrate ($SnCl_4 \cdot 5H_2O$) and oleic acid were utilized as additives to facilitate the formation of Na_2SnF_6. Analytical reagent (AR) grade powders of sodium fluoride with two different grain sizes were purchased from Sigma Aldrich (≥99%) and Alfa Aesar (≥99.99%). $SnCl_4 \cdot 5H_2O$ and oleic acid also were purchased from Sigma Aldrich and used as-purchased.

The chemical reaction between NaF and $SnCl_4 \cdot 5H_2O$ was performed in methanol (organic solvent) to avoid the hydrolysis of Sn^{4+} in DI water. Due to the relatively low solubility of NaF in methanol (3.28 g L^{-1} at 20 °C (ref. 30)), oleic acid was added to increase the dispersion or solubility of NaF in methanol. Serving as a surfactant, oleic acid is expected to increase the number of effective nucleation centers for the formation of Na_2SnF_6. Henceforth, in the present manuscript, the chemical reactions will be referred to as an organic solvent (OS) route, in which methanol was used as the solvent to dissolve NaF, and a surfactant-assisted or coordination-ligand-assisted or (OS-ligand) route, in which methanol and oleic acid were used as the solvent system to dissolve NaF. In the OS route, NaF was added into methanol and stirred to dissolve or disperse salt and 10–15 minutes later, $SnCl_4 \cdot 5H_2O$ was added to the solution. Once $SnCl_4 \cdot 5H_2O$ was added to the solution, a white precipitate formed immediately according to the following reaction (1),

$$6NaF + SnCl_4 \cdot 5H_2O \rightarrow Na_2SnF_6\downarrow + 4NaCl + 5H_2O \quad (1)$$

After stirring the mixed solution for around 30 minutes, the white precipitate was separated out from the solution through centrifugation at 9000 rpm for 5 min. The precipitated solid was rinsed two times with 10–10 mL methanol and dried in oven at 70 °C overnight. The surfactant-assisted OS route followed a similar procedure, with the exception of adding oleic acid to the methanol prior to dissolving the salts (NaF). The volume of oleic acid used was 1/16 of the methanol volume. First, the reaction conditions were optimized to completely immobilize NaF into Na_2SnF_6 and then, evaluate the effect of reaction temperature on reaction yield and reaction temperature as follows.

2.1.1. Solution-based immobilization of NaF into MHP. The methodology underlying the total immobilization of salt waste (NaF) into a MHP involves converting the entire amount of pretreated alkali fluoride salts into a crystalline waste form through a chemical reaction with an appropriate reagent. A small-scale reaction was performed by dissolving ~0.904 g (21.53 mmol) NaF with a grain size of 5–8 μm in 200 mL of methanol and reacting it with a stoichiometric amount of ~1.258 g (3.588 mmol) $SnCl_4 \cdot 5H_2O$ at 60 °C in the OS-route. Similarly, the same amount of NaF was dissolved in 100 mL methanol along with 6.25 mL oleic acid (1/16th of the methanol volume) and reacted with a stoichiometric amount of $SnCl_4 \cdot 5H_2O$ at 60 °C in the OS-ligand route. The phase confirmation in Fig. S1(a) and (b) (see SI Data) shows a minor contribution from unreacted NaF along with Na_2SnF_6 diffraction peaks. The presence of unreacted NaF shows incomplete immobilization. To achieve complete salt immobilization, the precipitate was further added in the remaining supernatant and reacted with additional 20% $SnCl_4 \cdot 5H_2O$. After further reaction with additional $SnCl_4 \cdot 5H_2O$ for 30 minutes, the obtained precipitate was filtered and dried followed by further structural characterization. Fig. S1(c) and (d) show that the diffraction maxima align with the PDF reference pattern (01-080-1155) of Na_2SnF_6. These results indicate that a 20% excess of $SnCl_4 \cdot 5H_2O$ is sufficient to achieve full immobilization of NaF into MHP as Na_2SnF_6.

2.1.2. Solution-based immobilization of NaF with varying grain sizes into MHP. The overall process of precipitation or co-precipitation involves the dissolution of reactants, nucleation of the solid phase from solution, and subsequent crystal growth. However, the dissolution rate of salt waste such as NaF in methanol is notably limited. Therefore, it is essential to investigate the various factors that may significantly influence the dissolution behavior of salt waste, as this could reduce methanol consumption and enhance the cost-effectiveness of the immobilization process. In particular, understanding the effect of salt grain size on its dissolution rate, nucleation behavior, and reaction yield would offer valuable insights for applications in the nuclear industry. Therefore, in addition to using NaF with grain sizes of a few microns, larger-grained NaF (of the order of a few hundred microns), and NaF with grain sizes of a few hundred nanometers has also been employed for salt waste immobilization. The nano-sized NaF powders were obtained by high energy ball milling of as-purchased micron-sized NaF to refine the particle size. To immobilize coarser powders of sodium fluoride (NaF) into Na_2SnF_6 in the OS-route, coarser powders of ~0.181 g NaF (4.31 mmol) were dissolved in 200 mL methanol and reacted at 60 °C with a non-stoichiometric amount of ~0.302 g $SnCl_4 \cdot 5H_2O$ (0.718 mmol). Similarly, the same amount of NaF was dissolved in 100 mL methanol along with 6.25 mL oleic acid (1/16th of the methanol volume) and reacted with the same amount of $SnCl_4 \cdot 5H_2O$ in the OS-ligand route. The white precipitates obtained through the OS route and OS-ligand route weighed approximately 0.171 g and 0.187 g, respectively. Accordingly, the reaction yield for immobilizing NaF into Na_2SnF_6 was estimated to be 85.5% and 93.5% in OS and OS-ligand routes, respectively, relative to the targeted product mass of 0.2 g. Similarly, 0.904 g of NaF powder (*i.e.*, five times that used for the coarser NaF powder) with a grain size of 5–8 μm and 100–200 nm were dissolved in 200 mL and 150 mL of methanol. The reactions were performed at 60 °C with a non-stoichiometric amount of $SnCl_4 \cdot 5H_2O$. The corresponding reaction times were 30 and 45 minutes. The methanol volume was reduced for the finer powder, and the reaction duration was increased to offset the decreased solvent quantity. In the OS-ligand route, the same amount of powder was dissolved in 100 mL and 75 mL volume of methanol and the reaction was performed under the same conditions with the help of oleic acid. In the OS-route, the reaction yield for 5–8 μm and 100–200 nm sized NaF powders was measured to be 85.4% and 87%, respectively. In the OS-ligand route, the reaction yield increased to 94.03% and 97.2%, respectively.

2.1.3. Solution-based immobilization reaction at different temperatures. The reaction was conducted at different temperatures such as 35 °C and room temperature (RT) to assess the impact of temperature, as room-temperature processing can significantly enhance cost-effectiveness. The immobilization of 0.904 g of NaF with 5–8 μm grain size was performed at 35 °C with a non-stoichiometric amount of $SnCl_4 \cdot 5H_2O$. The reaction time and amount of methanol were similar to those in the previous reaction at 60 °C. The reaction yield was found to be 84.2% and 93.3% in OS and OS-ligand routes, respectively. Similarly, 0.226 g of NaF with 5–8 μm grain size was added into 50 mL methanol and reacted with excess $SnCl_4 \cdot 5H_2O$ (0.377 g ∼120%). The reaction was performed at RT for 1 h with continuous mixing through a magnetic stirrer. In the OS-ligand approach, 50 mL of methanol was mixed with 3.2 mL of oleic acid at a 16 : 1 ratio, followed by the addition of 1.13 g of NaF (26.9 mmol) into the methanol–oleic acid solution. Excess $SnCl_4 \cdot 5H_2O$ (1.887 g ∼120%) was added into the solution and further reaction was performed at RT for 2 h. The reaction yield of NaF immobilization into Na_2SnF_6 at RT was found to be 96.8% and 91.2% in OS and OS-ligand routes, respectively.

2.2. Phase and microstructure characterization

The crystal structure of dried powders was analyzed through X-ray diffraction (XRD) using a Malvern Panalytical Empyrean system. The diffraction patterns were collected over a 2θ range of 15° to 80°, with a step size of 0.013°, using a conventional copper-K_α radiation source operated at 40 kV and 40 mA. The crystallographic orientation of synthesized powders was analyzed through Rietveld refinement of diffraction patterns using Fullprof-2005 software. Initially, the background was selected through a linear interpolation method using the Win-Plotr tool. The pseudo-Voigt function was employed to fit the background and diffraction peaks, respectively.[31] The microstructural investigation was conducted through a SEM equipped with a Schottky thermal field emitter using an FEI Versa 3D Dual Beam system. Secondary electron (SE) imaging was recorded using an Everhart–Thornley Detector (ETD) while energy-dispersive spectroscopy (EDS) was performed to probe the micro-chemistry of the synthesized powder. EDS imaging was recorded using a silicon drift detector (Oxford instruments, UK). The as-synthesized MHP powders were dispersed onto a carbon tape and coated with a thin conductive layer of gold and platinum (a few nanometers thick) to prevent charging during SEM characterization. The thermal stability of the prepared MHP was evaluated by TGA. The measurements were performed using a DSC/TGA apparatus (SDT650, TA Instruments, DE, USA) with horizontal dual beams. Approximately 20–30 mg of sample powders were loaded in a standard alumina crucible (90 μL) and heated to 1000 °C with a heating rate of 10 °C min^{-1}. The measurement was performed in an argon environment maintained by a steady flow of 50 mL min^{-1}.

2.3. Consolidation of Na_2SnF_6

The as-synthesized MHP powders through OS and OS-routes at RT were consolidated into monolithic cylindrical pellets using spark plasma sintering (SPS) (Dr Sinter SPS 211-LX, Fuji, Saitama, Japan) in an argon environment. A low temperature consolidation process was optimized using DMSO as an additive to enhance diffusion and particle bonding during the SPS process at 200 °C. The powders were loaded into a graphite die set and sandwiched between two graphite punches. To prevent powder–die interaction and to facilitate easy removal from the die set, the powders were covered with graphite paper in a cup-like structure. This innovative cold sintering process (CSP) was conducted at 200 °C for 15 min under an applied pressure of 60 MPa, with heating and cooling rates of 25 °C min^{-1}.

3. Results and discussion

3.1. Structural analysis and phase behavior

Phase confirmation of the synthesized white precipitates in various reactions was carried out using XRD. Fig. 1 shows the representative diffraction patterns of the as-synthesized Na_2SnF_6. In both cases, either the OS route (Fig. 1(a)) or OS-ligand route (Fig. 1(c)), the diffraction patterns show that the primary phase corresponds to a tetragonal $P4_2/mnm$ structure, matching the PDF reference pattern (01-080-1155) for Na_2SnF_6.[32] Interestingly, some reactions at higher temperatures using micron-sized NaF show that the secondary phase belongs to a hexagonal symmetry of the $P321$ space group, referred to the PDF reference pattern (00-047-1082) for the secondary phase of Na_2SnF_6. This β-phase of Na_2SnF_6 was also reported by Grannec *et al.*, who observed that it forms under rapid thermal quenching and is a high-temperature phase that remains metastable at room temperature, eventually transforming the $P4_2/mnm$ structure.[33] In contrast, the reaction kinetics in the case of NaF with coarser powders (120–150 μm) was slower, although the reaction was carried out using only one-fifth of the amount of salts in the same volume of methanol (200 mL).

Therefore, in the OS-route, the β-phase of Na_2SnF_6 was observed only for the reaction in which NaF with 5 μm immobilized at 60 °C. In the OS-ligand route, the reaction kinetics was sufficiently fast to form the metastable phase for the reactions using micron-sized NaF at 35 and 60 °C, and nano-sized NaF at 60 °C, consistent with the ligand-assisted nucleation with fast reaction kinetics at higher temperature as compared with room temperature. However, nano-sized NaF (100–200 nm) was used in a smaller volume of methanol without a ligand in the OS route at 60 °C, and a longer duration was required for the reaction, resulting in Na_2SnF_6 crystallized in the tetragonal structure despite higher temperature and finer particle size. This indicates that the formation of the metastable β-phase is strongly influenced by reaction time in addition to governing solely by reaction kinetics alone. It must be noted that the diffraction patterns in Fig. 1(b) and (d) clearly show no impurity peaks of unreacted NaF and NaCl present in synthesized powders.

The diffraction patterns of synthesized MHPs were further analyzed through Rietveld refinement. Fig. 2 presents the refined structures of Na_2SnF_6 synthesized at 35 °C through the OS route and OS-ligand route. The diffraction peaks of Na_2SnF_6 synthesized through the OS route were fitted based on tetragonal symmetry of the trirutile type $P4_2/mnm$ 136 space group with $Z = 2$. The cations occupy octahedral sites, and Na^+ is coordinated with six F^- atoms to form NaF_6 octahedra and Sn^{4+} is bonded to six F^- atoms to form SnF_6 octahedra as shown in Fig. 2(c). Fig. 2(b) presents the refined structures of Na_2SnF_6 synthesized through the OS-ligand route with the introduction of both α and β-phases. The β-phase can be described by trigonal symmetry of the Na_2SiF_6-type ($P321$ space group) with $Z = 3$ in space group no. 150. In this hexagonally crystallized

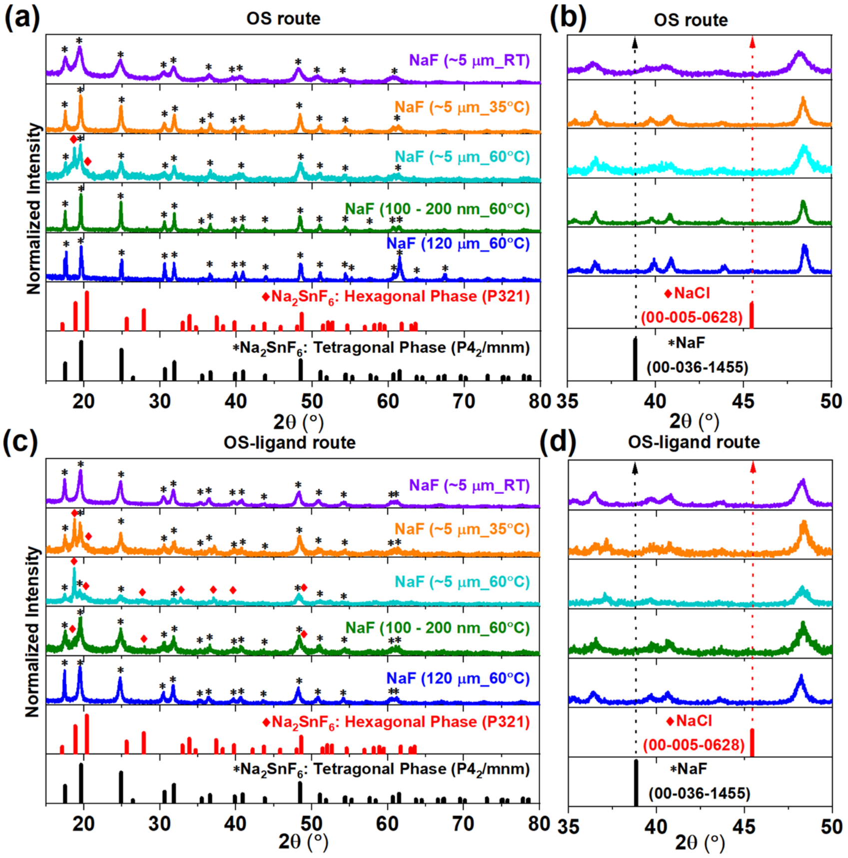

Fig. 1 XRD patterns of Na_2SnF_6 synthesized through (a) OS and (c) OS-ligand routes under various reaction conditions at different temperatures (RT, 35 °C and 60 °C) with different particle sizes (coarse, fine and nano-sized NaF). Enlarged patterns in (b) OS and (d) OS-ligand routes show no impurity of NaF and NaCl.

Na_2SnF_6 structure, two crystallographically independent Na^+ ions are coordinated with six F^- ions to form distorted NaF_6 octahedra. The structure also contains two Sn^{4+} sites, each coordinated by six F^- ions to form two distinct $[SnF_6]^{2-}$ octahedra.[34] Table 1 shows the refined structural parameters of synthesized Na_2SnF_6. The lattice parameters in all reactions were found to be smaller in the OS route than in the OS-ligand route. This can be attributed to the fact that, in the OS-ligand route, faster and more homogeneous nucleation produces crystals with fewer vacancies, resulting in slightly larger lattice parameters. Qiao *et al.* also reported that the unit cell of synthesized $LiFePO_4$ powders was larger when prepared using a surfactant-assisted chemical route compared to samples synthesized without a surfactant.[35] The XRD results clearly show that the reactions enriched with $SnCl_4\cdot5H_2O$ in both OS and OS-ligand routes successfully converted NaF into Na_2SnF_6. The

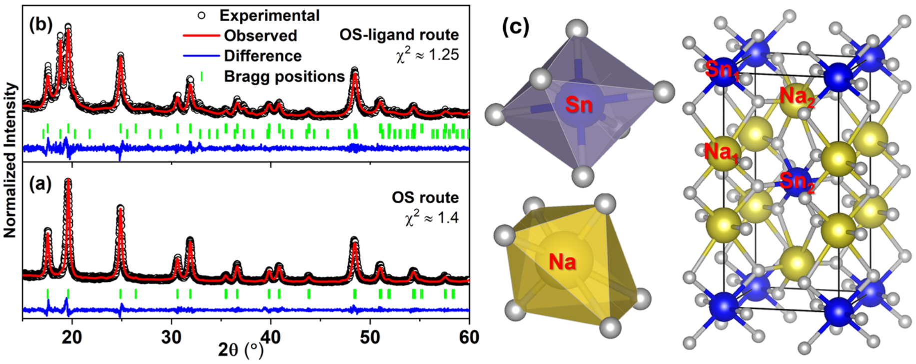

Fig. 2 Refined XRD patterns of Na_2SnF_6 synthesized through (a) OS route and (b) OS-ligand route at 35 °C and (c) crystal structure of Na_2SnF_6 crystallized with tetragonal symmetry of trirutile type *P*4$_2$/*mnm*.

different reaction conditions indicate that rapid precipitation or high supersaturation, driven by elevated reaction temperatures, particle size and ligand-assisted synthesis, promotes the crystallization of the metastable phase of Na_2SnF_6.

3.2. Microstructural and microchemical analysis

SEM was performed to examine the microstructure and microchemistry of the as-synthesized Na_2SnF_6. Fig. 3(a_1–e_1) and (a_2–e_2) show the microstructure of synthesized Na_2SnF_6 *via* the OS route and OS-ligand route, respectively. The powders appear to have good crystallinity, which exhibit agglomerated grain clusters ranging from hundreds of nanometers to a few micrometers in various reactions. Generally, grain clusters obtained from the OS-route are larger than that obtained from the OS-ligand synthesis route.

SEM analysis concludes that the relatively smaller agglomerated grain clusters of MHP result from the increased number of nucleation centers provided by the surfactant, which hinders grain agglomeration. This can be explained by Ostwald ripening in which the large crystals grow at the expense of smaller ones due to the difference in solubility.[36] Yang *et al.* also reported that the use of oleic acid decreased the grain size of $LiMnO_4$ and increased the homogeneity.[37] As a result, the crystals remained smaller compared to those synthesized *via* the OS route under identical reaction conditions. Since particle morphology is controlled by the nucleation rate, supersaturation and crystal growth kinetics, increasing the reaction rate or supersaturation at higher reaction temperature or lower amount of used methanol helps to produce spherical homogeneous nanoparticles.[38] Na_2SnF_6 synthesized at 60 °C for 30 min using 5 μm NaF (0.904 g) in 200 mL and 100 mL methanol *via* the OS and OS-ligand routes, respectively, exhibits a spherical morphology as shown in Fig. 3(c_1 and c_2). In the OS route, nearly 1 μm spherical particles are obtained, whereas the OS-ligand route yields ~1 μm spherical clusters composed of 200–300 nm spherical primary grains. In contrast, Na_2SnF_6 synthesized under similar reaction conditions using 120 μm NaF (0.181 g) in 200 mL and 100 mL methanol (OS and OS-ligand routes, respectively) shows the formation of flower-like nanostructures consisting of 100–400 nm crystallites as shown in Fig. 3(a_1 and a_2). These observations clearly demonstrate the effect of solution supersaturation on the nucleation and growth behavior of Na_2SnF_6. A high degree of supersaturation promotes a rapid and homogeneous burst of nucleation, resulting in the formation of spherical particles. Similarly, Na_2SnF_6 synthesized at 35 °C for 30 min also exhibits nearly spherical particles. In contrast, synthesis performed at room temperature for 1–2 h leads to irregularly shaped, agglomerated particles with sizes in the range of 1–5 μm, as shown in Fig. 3(e_1 and e_2).

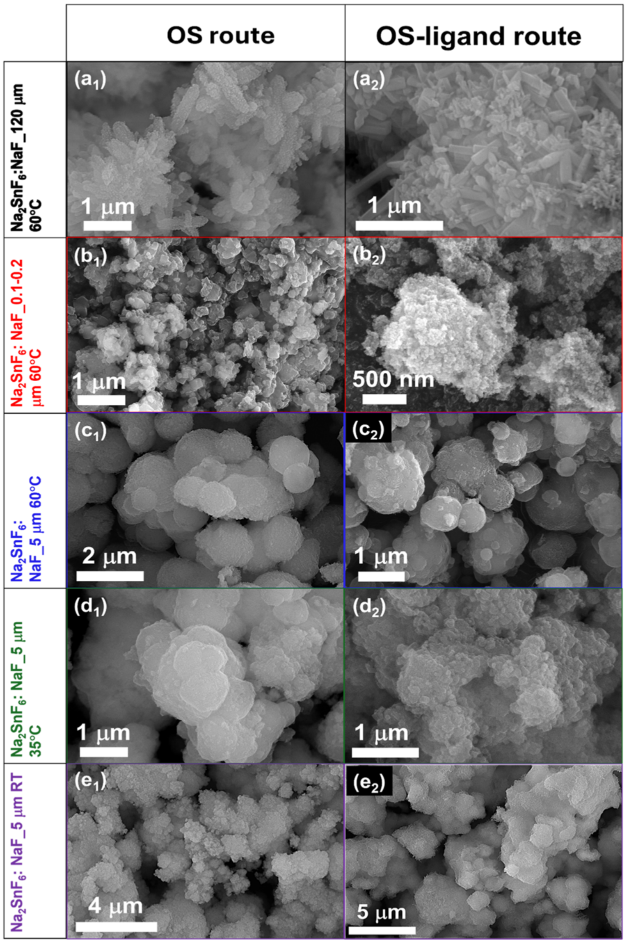

Fig. 3 SEM images of synthesized Na_2SnF_6 in various reactions from the (a_1–e_1) OS-route and (a_2–e_2) OS-ligand route.

EDS mapping shown in Fig. 4 and 5 validates the microchemistry in MHPs synthesized by both synthesis routes under various reaction conditions. Table 2 presents the EDS-derived empirical formula. Fig. 4 (OS route) and Fig. 5 (OS-ligand route) show the uniform elemental distribution throughout the

Table 1 The refined structural parameters of synthesized Na_2SnF_6

MHP (Na_2SnF_6)	OS route	OS-ligand route
NaF_120 μm (60 °C)	$a = b = 5.057$ Å & $c = 10.112$ Å [100% tetragonal]	$a = b = 5.071$ Å & $c = 10.148$ Å [100% tetragonal]
NaF_5 μm (60 °C)	$a = b = 5.067$ Å, & $c = 10.099$ Å [61% tetragonal] $a = b = 9.412$ Å & $c = 5.181$ Å [39% hexagonal]	$a = b = 5.073$ Å, $c = 10.103$ Å [29% tetragonal] $a = 9.423$ Å, $c = 5.191$ Å [71% hexagonal]
NaF_100–200 nm (60 °C)	$a = b = 5.063$ Å, & $c = 10.114$ Å [100% tetragonal]	$a = b = 5.073$ Å, $c = 10.110$ Å [73.7% tetragonal] $a = b = 9.415$ A, $c = 5.309$ A [26.3% hexagonal]
NaF_5 μm (35 °C)	$a = b = 5.064$ Å, & $c = 10.114$ Å [100% tetragonal]	$a = b = 5.073$ Å, $c = 10.113$ Å [51% tetragonal] $a = 9.435$ Å, $c = 5.185$ Å [49% hexagonal]
NaF_5 μm (RT)	$a = b = 5.066$ Å, & $c = 10.102$ Å [100% tetragonal]	$a = b = 5.069$ Å, & $c = 10.104$ Å [100% tetragonal]

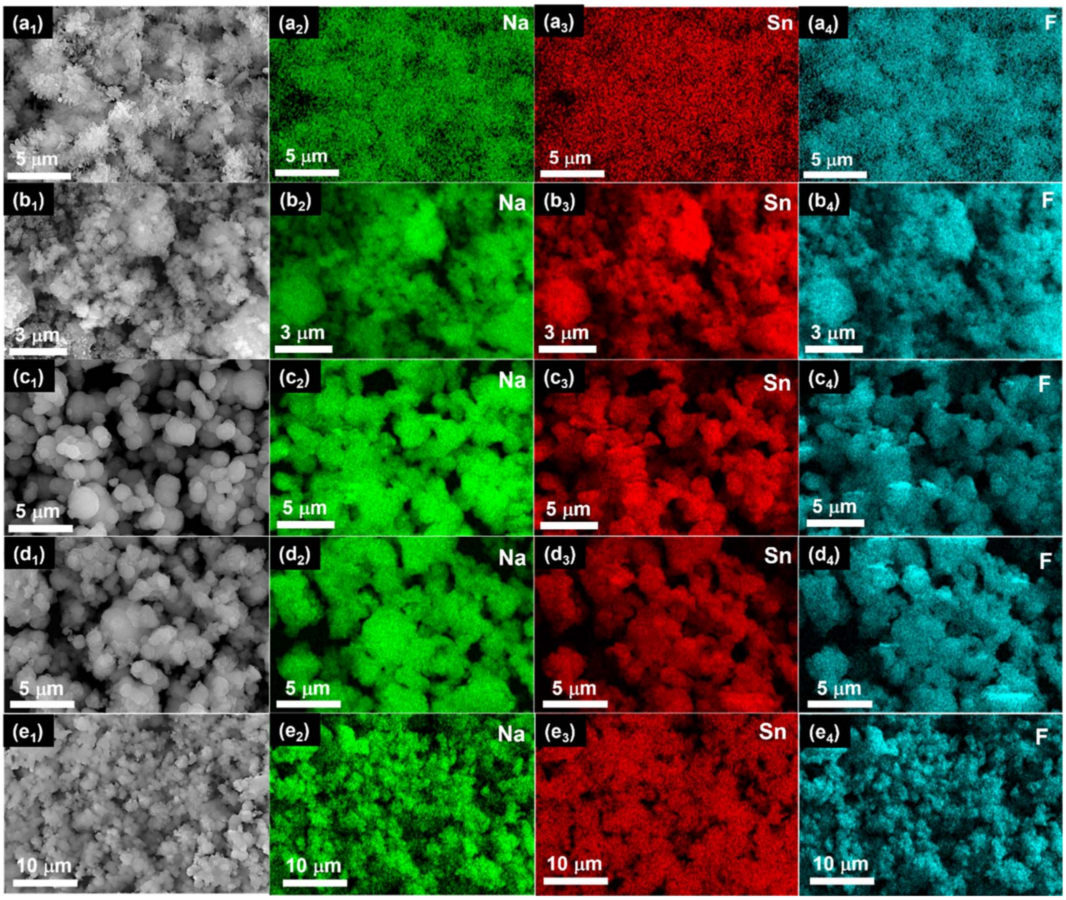

Fig. 4 EDS elemental mapping of Na, Sn, and F in synthesized Na_2SnF_6 in the OS-route under various reaction conditions: (a) NaF_120 μm (60 °C), (b) NaF_5 μm (60 °C), (c) NaF_100–200 nm (60 °C), (d) NaF_5 μm (35 °C), and (e) NaF_5 μm (RT).

powder sample. Overall, Na_2SnF_6 synthesized *via* the OS route exhibits a higher concentration of Na vacancies compared to that prepared by the OS–ligand route. This observation is consistent with the XRD results and supports the smaller unit-cell parameters estimated for the MHP synthesized through the OS route. EDS analysis yielded an atomic ratio of Na : Sn : F close to the composition Na_2SnF_6 within error due to limitations of EDS for light elements.

3.3. Thermal stability of MHPs by thermogravimetric analysis

Fig. 6(a) and (b) present the thermogravimetric analysis (TGA) results illustrating the thermal stability of the synthesized MHPs. Upon heating up to 400 °C, Na_2SnF_6 synthesized *via* the OS route at 60 °C using NaF with grain sizes of 120 μm, 5 μm and 100–200 nm exhibits weight losses of approximately 2.0%, 2.1%, and 2.0%, respectively. In addition, samples synthesized at 35 °C and room temperature (RT) using 5 μm NaF show weight losses of 2.2% and 2.25%, respectively. These minor weight losses are attributed to the removal of adsorbed moisture and volatile impurities. Similarly, in the OS-ligand route, Na_2SnF_6 synthesized at 60 °C using NaF with grain sizes of 120 μm, 5 μm and 100–200 nm undergoes weight losses of approximately 2.0%, 2.4%, and 2.6%, respectively; whereas samples synthesized at 35 °C and RT using 5 μm NaF exhibit weight losses of 1.4% and 2.5%, respectively. Overall, the MHPs synthesized *via* the OS-ligand route show a comparable thermal stability trend to those prepared by the OS route. A distinct weight-loss event was observed in the range of 340–360 °C, which is attributed to the decomposition and removal of residual oleic acid. The TGA results confirm that the synthesized Na_2SnF_6 exhibits excellent thermal stability up to 400 °C, irrespective of reaction temperature, NaF grain size, or the presence of surfactants.

3.4. Impacts of synthesis conditions on the reaction yield and scalability

Fig. 7 illustrates the impacts of temperature, grain size, and surfactant addition on the efficiency of NaF immobilization into Na_2SnF_6. Using 0.181 g of coarse-grained NaF (120–150 μm), effective immobilization was achieved at 60 °C with a reaction yield of 85.5% in 200 mL of methanol. Upon the addition of a surfactant, the methanol volume was reduced to 100 mL, while the reaction yield increased to 93.5% under the same conditions. When the grain size of NaF was reduced to 5–8 μm, a large amount of salt (1.25 times that of the coarser-grained NaF, *i.e.*, 0.225 g) was immobilized at RT using only 50 mL of

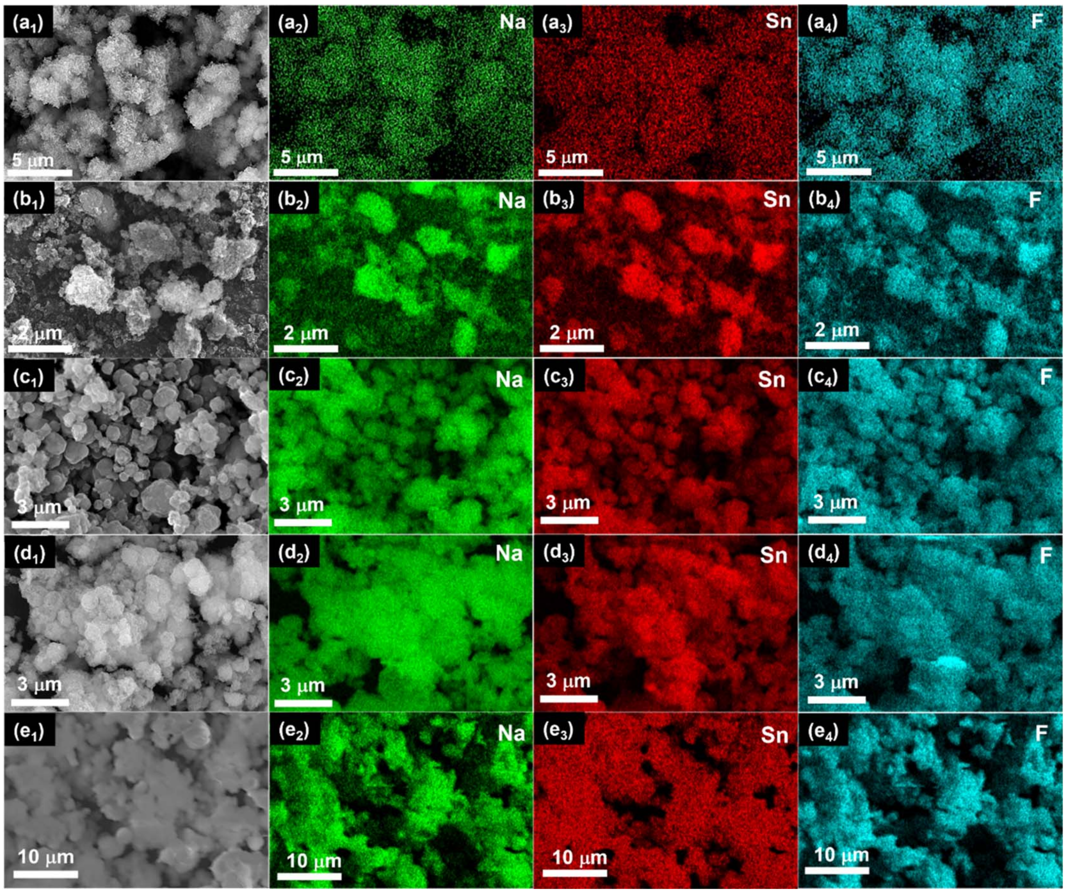

Fig. 5 EDS elemental mapping of Na, Sn, and F in synthesized Na_2SnF_6 in the OS-route under various reaction conditions: (a) NaF_120 µm (60 °C), (b) NaF_5 µm (60 °C), (c) NaF_100–200 nm (60 °C), (d) NaF_5 µm (35 °C), and (e) NaF_5 µm (RT).

Table 2 EDS-derived empirical formula for all-synthesized Na_2SnF_6

MHP (Na_2SnF_6)	OS route	OS-ligand route
NaF_120 µm (60 °C)	$Na_{1.88}SnF_{6.02}$	$Na_{2.01}SnF_6$
NaF_5 µm (60 °C)	$Na_{1.98}SnF_{6.02}$	Na_2SnF_6
NaF_100–200 nm (60 °C)	Na_2SnF_6	$Na_{2.03}SnF_{6.08}$
NaF_5 µm (35 °C)	$Na_{1.92}SnF_{6.06}$	$Na_2SnF_{6.02}$
NaF_5 µm (RT)	Na_2SnF_6	$Na_{1.99}SnF_6$

methanol, with a high reaction yield of 96.8% albeit with an extended reaction time of 1 h.

Scaling up the same micron-sized feedstock to 5× (0.904 g) resulted in successful immobilization into MHP with reduced reaction yields of 84.2% and 85.4% at 35 °C and 60 °C, respectively. Further reducing the salt grain size to the nanoscale (100–200 nm) improved the reaction yield to 87% for the 5× scale (0.904 g) using 150 mL of methanol. Notably, the addition of a surfactant enhanced the efficiency of this scaled-up process, increasing the reaction yield to 97.2% while reducing the methanol requirement to only 75 mL, as shown in Fig. 7(a). Similar trends were observed for the micron-sized NaF under ligand-assisted synthesis conditions, where reaction yields exceeding 90% were achieved upon scaling the salt quantity to 5×, 5×, and 6.25× at 35 °C, 60 °C, and room temperature, respectively. Collectively, these results demonstrate a cost-effective, solution-based strategy for the immobilization of salt waste and highlight its strong potential for scalable processing. This systematic study concludes that the presence of a surfactant not only enhances the solubility of NaF in methanol but also facilitates the nucleation of Na_2SnF_6 by lowering the energy barrier and providing additional nucleation sites. Therefore, the reaction yield was found to be increased in the OS-ligand route compared the OS route as shown in Fig. 7(b). As grain size directly affects the solubility of NaF in methanol, larger-grained salt requires approximately five times more methanol than micron-grained salt to dissolve and immobilize the same amount of NaF as the solid dissolution rate is proportional to the surface area available for dissolution. Therefore, grinding the salt particles into fine particles helps to minimize the consumption of methanol. Fig. 7(c) clearly shows that the decreasing salt grain size helped to scale up the immobilization process with increased reaction yield in both OS and OS-ligand routes. Elevated reaction temperatures slightly improve the solubility of NaF and increase kinetic energy, promoting faster formation and nucleation of Na_2SnF_6. This reflects in increasing reaction yield from 35 to 60 °C as shown in Fig. 7(d). However, the reaction can also proceed effectively at

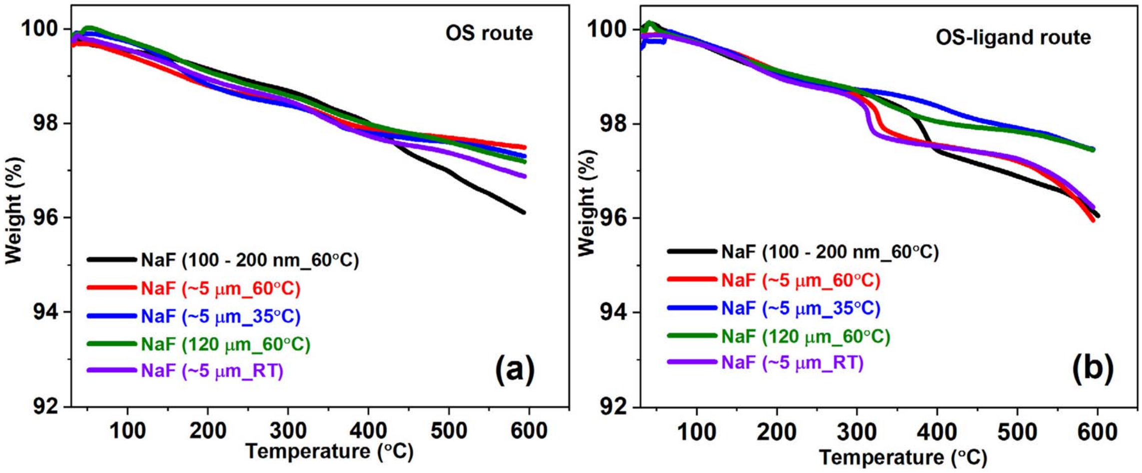

Fig. 6 Thermal stability as evaluated by TGA testing (up to 600 °C with a ramping rate of 10 °C min^{-1}) for the synthesized Na_2SnF_6 samples under different reaction conditions *via* the (a) OS-route and (b) OS-ligand route.

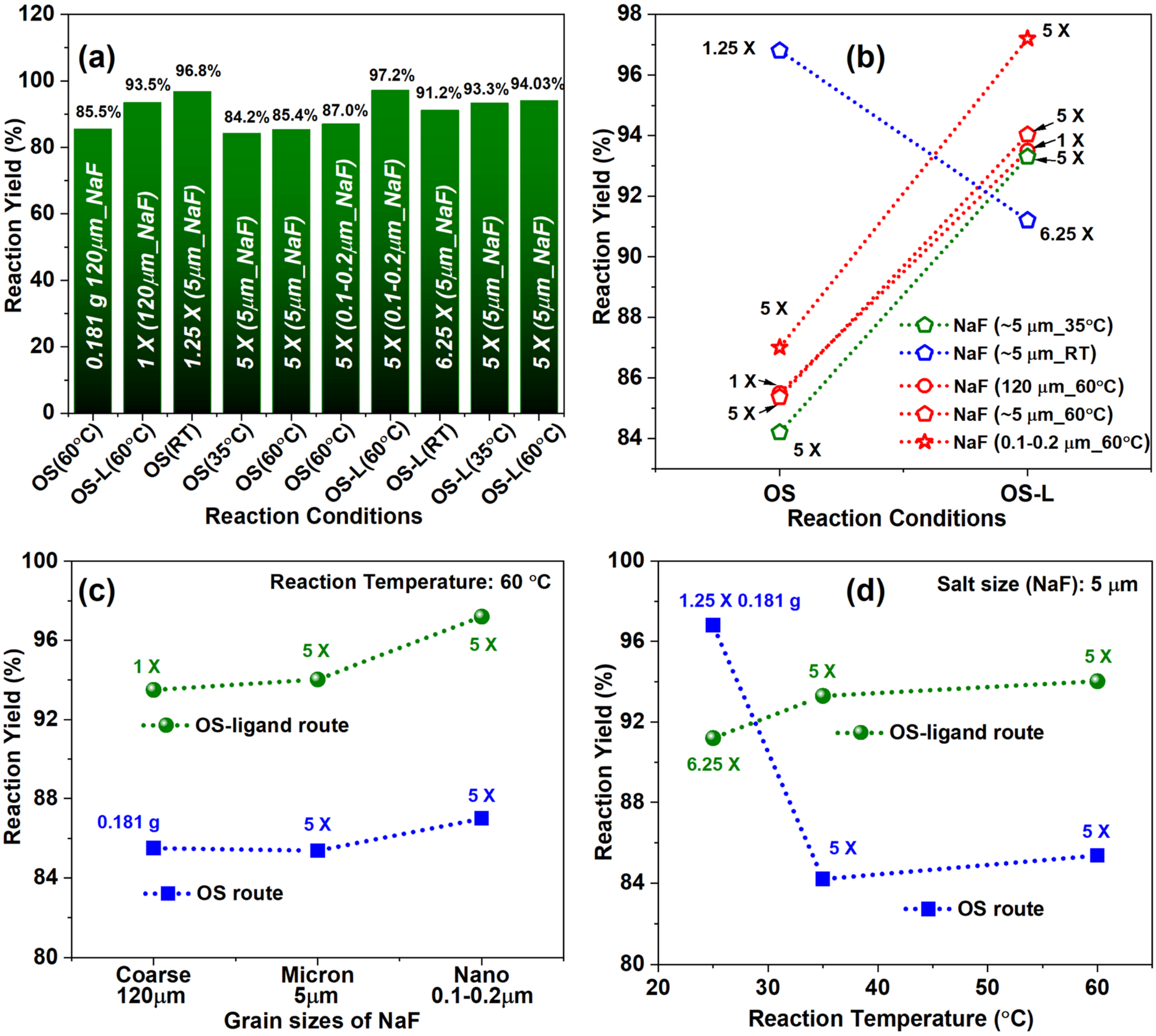

Fig. 7 (a) A comparison among reaction yields with respect to studied variable parameters of the immobilization process, (b) the effect of a ligand on the reaction yield, (c) the effect of grain size on reaction yield, and (d) the effect of reaction temperature on reaction yield.

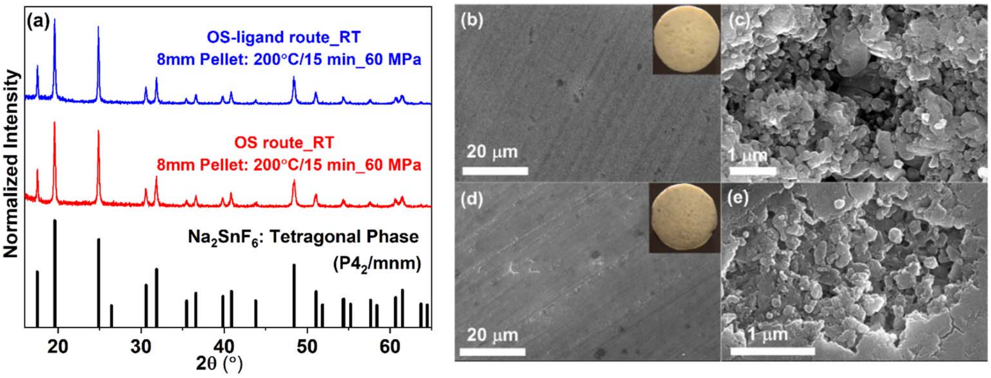

Fig. 8 (a) XRD patterns of monolithic pellets of Na_2SnF_6 synthesized at RT through OS and OS-ligand routes. (b–e) The SEM images of monolithic pellets of Na_2SnF_6 synthesized at RT through OS and OS-ligand routes, respectively.

room temperature, with longer processing times compensating for the lower kinetics, making it suitable for industrial-scale applications.

3.5. Consolidation and densification of Na_2SnF_6 into monolithic waste forms

It is essential to consolidate the MHP into the dense pellets as waste forms for the permanent immobilization of the waste elements. Conventional high-temperature sintering is unsuitable for this material due to the risk of MHP degradation or loss. A cost-effective sintering process (CSP) is required to fabricate monolithic, densified Na_2SnF_6 samples at temperatures significantly lower than the temperature leading to the loss of highly volatile waste elements. To overcome this limitation, a novel cold sintering process (CSP) was developed. Assisted by SPS, the CSP employed dimethyl sulfoxide (DMSO) as a transient solvent to partially dissolve the synthesized Na_2SnF_6 and promote densification at low temperature. Initial attempts using deionized water or methanol as transient solvents were unsuccessful, as Na_2SnF_6 could not be effectively densified. In contrast, the addition of a few drops of DMSO into the Na_2SnF_6-loaded graphite die enabled effective cold sintering, resulting in pellets with densities reaching ~90% of the theoretical value.

The CSP was conducted at 200 °C for 15 min under an applied pressure of 60 MPa, with heating and cooling rates of 25 °C min^{-1}. The measured pellet densities were ~89% and ~91% of the theoretical density for Na_2SnF_6 synthesized at room temperature *via* the OS and OS-ligand routes, respectively. The enhanced densification is attributed to a dissolution–reprecipitation mechanism inherent to the cold sintering process, wherein partial dissolution of Na_2SnF_6 in DMSO facilitates elemental transport and atomic diffusion within the transient solvent phase. Consequently, the addition of a small amount of DMSO markedly improves pellet consolidation at temperatures as low as 200 °C, while preserving the structural integrity of the MHP phase. Fig. 8(a) presents the XRD patterns of the densified pellets, confirming the retention of the tetragonal Na_2SnF_6 phase. Fig. 8(b–e) show SEM images of the polished pellet surfaces prepared from Na_2SnF_6 synthesized at room temperature *via* the OS and OS-ligand routes, respectively, clearly illustrating particle bonding and neck formation achieved through the CSP. The homogeneous spatial distribution of Na, Sn, and F, as revealed by EDS elemental mapping (Fig. S2, SI), confirms that crystal chemistry remains chemically inert during the CSP.

4. Conclusion

In conclusion, the present study reports a cost-effective, scalable, and low-temperature solution-based approach for the immobilization of fluoride salt waste into a MHP-structured compound, *e.g.*, NaF as a representative system into Na_2SnF_6. The immobilization process addresses a critical need in nuclear waste management by enabling high fluoride loading (up to 57.4 wt%) with minimal byproduct formation. Systematic optimization of immobilization parameters including different reaction temperatures (60 °C, 35 °C, and RT), salt grain sizes (120 μm, 5 μm, and 100–200 nm), and the use of surfactants consistently yielded reaction efficiencies above 90%. Reducing grain size of salt and the addition of a surfactant significantly enhanced the reaction yield and reduced the methanol consumption. Structural and chemical characterization studies using XRD, SEM, EDS, and TGA confirmed the formation of thermally stable, homogeneously distributed Na_2SnF_6 with excellent crystallinity and elemental uniformity. Microstructural analysis of the synthesized waste forms revealed that the presence of a surfactant significantly enhanced the reaction yield by promoting additional nucleation sites for waste form precipitation and reducing grain agglomeration. An innovative cold sintering process integrated with SPS was developed, enabling the consolidation of synthesized Na_2SnF_6 at 200 °C while achieving 89–91% of the theoretical density and minimizing the loss of highly volatile waste elements, thereby demonstrating its practical viability as a waste form material.

Conflicts of interest

The authors declare that they have no known competing financial interests.

Data availability

All data supporting this article have been included in the manuscript. Additional data are available from the corresponding author upon reasonable request.

Supplementary information (SI) is available. See DOI: https://doi.org/10.1039/d6ta00002a.

Acknowledgements

This work was supported by a DOE ARPA-E program under the award number DE-AR0001615.

References

1 C. Le Brun, Molten Salts and Nuclear Energy Production, *J. Nucl. Mater.*, 2007, **360**, 1.

2 A. Coulon, D. Laurencin, A. Grandjean, C. Cau Dit Coumes, S. Rossignol and L. Campayo, Immobilization of Iodine into a Hydroxyapatite Structure Prepared by Cementation, *J. Mater. Chem. A*, 2014, **2**, 20923.

3 B. J. Riley, *et al.*, Iodine Solubility in a Low-Activity Waste Borosilicate Glass at 1000 °C, *J. Nucl. Mater.*, 2014, **452**, 178–188.

4 R. C. Ewing, Nuclear Waste Forms for Actinides, *Proc. Nat. Academy Sci.*, 1999, **96**(7), 3432–3439.

5 B. J. Riley, Glass Binder Development for a Glass-Bonded Sodalite Ceramic Waste Form, *J. Nucl. Mater.*, 2017, **489**, 42–63.

6 B. VanEmden, M. R. Thornber, J. Graham and F. J. Lincoln, The Incorporation Of Actinides In Monazite and Xenotime From Placer Deposits In Western Australia, *Can. Mineral.*, 1997, **35**, 95–104.

7 F. Lu, T. Yao, Y. Danon, J. Zhou, R. C. Ewing and J. Lian, Radiation Stability of Spark-Plasma-Sintered Lead Vanadate Iodoapatite, *J. Am. Ceram. Soc.*, 2015, **98**(10), 3361–3366.

8 G. D. DelCul, R. D. Hunt and W. S. Aaron, *Complete tests to produce cermet and grout waste forms using surrogate oxide and nitrate powders*, NTRD-MRWFD-2018-000143, ORNL/SPR-2018/877, Oak Ridge National Laboratory, 2018.

9 B. J. Riley, J. McFarlane, G. D. DelCul, J. D. Vienna, C. I. Contescu and C. W. Forsberg, Molten Salt Reactor Waste and Effluent Management Strategies: A Review, *Nucl. Eng. Des.*, 2019, **345**, 94.

10 J. Wei, X. Shu, W. Han, R. Tan, M. Wen, Z. Li and X. Lu, Immobilize Simulated Am–Np–RE–Pu Product Waste from Trialkyl Phosphine Oxide Process in Natural Granite-Based Aluminum Silicate Glass or Glass–Ceramic, *J. Mater. Chem. A*, 2025, **13**, 15841.

11 S. Zhou, X. Liu, Z. Qian, Y. Qiao, B. Yu, L. Li, S. Wang and Q. Qin, Preparation and Characterization of Phosphate Glass – Ceramic Wasteform with Strontium Fluoride, *J. Radioanal. Nucl. Chem.*, 2021, **328**, 217.

12 X. Liu, Y. Qiao, Z. Qian and H. Ma, Research on Chemical Durability of Iron Phosphate Glass Wasteforms Vitrifying SrF2 and CeF3, *J. Nucl. Mater.*, 2018, **508**, 286–291.

13 X. Liu, Y. Qiao, Z. Qian, S. Zhou, L. Li, J. Ma, S. Wang, Q. Qin and Q. Zhang, Structure and Corrosion Mechanism of Iron Phosphate Glass with Strontium from Electrochemical Reprocessing, *J. Hazard. Mater. Adv.*, 2021, **4**, 100027.

14 X. Liu, Q. Zhang, Y. Wei, Y. Qiao, X. Duan, L. Li, Y. Chen and Z. Qian, Vitrification of Cerium(III) Fluoride in Iron Phosphoborate Glasses: A Study on Redox, Structure, and Stability, *Ceram. Int.*, 2024, **50**(20), 38435–38444.

15 H. Jena, B. K. Maji, R. Asuvathraman and K. V. G. Kutty, *Mater. Chem. Phys.*, 2015, **162**, 188–196.

16 C. T. Moynihan and S. R. Loehr, Chemical Durability of Fluoride Glasses, *Mater. Sci. Forum*, 1991, **32–33**, 243.

17 C. J. SIMMONS and J. H. SIMMONS, Chemical Durability of Fluoride Glasses: I, Reaction of Fluorozirconate Glasses with Water, *J. Am. Ceram. Soc.*, 1986, **69**, 661.

18 B. J. Riley, J. O. Kroll, J. A. Peterson, D. A. Pierce, W. L. Ebert, B. D. Williams, M. M. V Snyder, S. M. Frank, J. L. George and K. Kruska, Assessment of Lead Tellurite Glass for Immobilizing Electrochemical Salt Wastes from Used Nuclear Fuel Reprocessing, *J. Nucl. Mater.*, 2017, **495**, 405.

19 B. J. Riley, B. T. Rieck, J. S. Mccloy, J. V Crum, S. K. Sundaram and J. D. Vienna, Tellurite Glass as a Waste Form for Mixed Alkali – Chloride Waste Streams : Candidate Materials Selection and Initial Testing, *J. Nucl. Mater.*, 2012, **424**, 29.

20 B. J. Riley and S. Chong, Glass Waste Form Options for Rare-Earth Fi Ssion Products from Electrochemical Reprocessing, *J. Non. Cryst. Solids*, 2020, **545**, 120161.

21 B. J. Riley, D. A. Pierce, J. V. Crum, B. D. Williams, M. M. V Snyder and J. A. Peterson, Waste Form Evaluation for RECl3 and REOx Fission Products Separated from Used Electrochemical Salt, *Prog. Nuc. Energy*, 2018, **104**, 102–108.

22 I. W. Donald, B. L. Metcalfe, S. K. Fong, L. A. Gerrard, D. M. Strachan and R. D. Scheele, A Glass-Encapsulated Calcium Phosphate Wasteform for the Immobilization of Actinide-, Fluoride-, and Chloride-Containing Radioactive Wastes from the Pyrochemical Reprocessing of Plutonium Metal, *J. Nucl. Mater.*, 2007, **361**, 78.

23 F. Lu, Z. Dong, J. Zhang, T. White, R. C. Ewing and J. Lian, Tailoring the Radiation Tolerance of Vanadate-Phosphate Fluorapatites by Chemical Composition Control, *RSC Adv.*, 2013, **3**, 15178.

24 D. J. Gregg, E. R. Vance, P. Dayal, R. Farzana, Z. Aly, R. Holmes and G. Triani, Hot Isostatically Pressed (HIPed) fluorite glass-ceramic wasteforms for fluoride molten salt wastes, *J. Am. Ceram. Soc.*, 2020, **103**, 5454–5469.

25 S. A. L, H. Jena and S. Kumar, Studies on Nd Solubility in Ca 10 (PO 4) 6 F 2 and Its Borosilicate Glass Bonded Analogues Synthesized by Using CaF 2 Recovered from Spent Salt of Electro-Winning Process, *Ceram. Int.*, 2021, **47**, 31054.

26 C. Cao, S. Chong, L. Thirion, J. C. Mauro, J. S. McCloy and A. Goel, Wet Chemical Synthesis of Apatite-Based Waste Forms-A Novel Room Temperature Method for the Immobilization of Radioactive Iodine, *J. Mater. Chem. A*, 2017, **5**, 14331.

27 K. Yang, W. Zhu, S. Scott, Y. Wang, J. Wang, B. J. Riley, J. Vienna and J. Lian, Immobilization of Cesium and Iodine into Cs3Bi2I9 Perovskite-Silica Composites and

Core-Shell Waste Forms with High Waste Loadings and Chemical Durability, *J. Hazard. Mater.*, 2021, **401**, 123279.

28 K. Yang, W. Zhu, B. J. Riley, J. D. Vienna, D. Zhao and J. Lian, Perovskite-Derived Cs2SnCl6−Silica Composites as Advanced Waste Forms for Chloride Salt Wastes, *Environ. Sci. Technol.*, 2021, **55**, 7605–7614.

29 C. J. Bartel, C. Sutton, B. R. Goldsmith, R. Ouyang, C. B. Musgrave, L. M. Ghiringhelli and M. Scheffler, New Tolerance Factor to Predict the Stability of Perovskite Oxides and Halides, *Sci. Adv.*, 2019, **5**(2), 1.

30 F. G. Germuth, The Solubilities of Alkali Bromides and Fluorides in Anhydrous Methanol, Ethanol, and Butanol, *J. Franklin Inst.*, 1931, **212**(3), 343–349.

31 S. K. Sharma, V. Grover, R. Shukla, A. Hussain, A. Mishra, R. C. Meena and P. K. Kulriya, Evidence of Improved Tolerance to Electronic Excitation in Nanostructured Nd2Zr2O7, *J. Appl. Phys.*, 2021, **129**, 115902.

32 G. Benner and R. Hoppe, Zur struktur von Na2SnF6, *J. Fluorine Chem.*, 1990, **48**(2), 219–227.

33 J. Grannec, L. Fournès and P. Lagassié, X-Ray and Mössbauer Evidence for a High Temperature Form of Na2SnF6, *Mater. Res. Bull.*, 1990, **25**, 1035–1041.

34 A. Zalkin, J. D. Forrester and D. H. Templeton, The crystal structure of sodium fluorosilicate, *Acta Cryst.*, 1964, **17**, 1408–1412.

35 Y. Qiao, Y. Liu, J. Zhu, P. Jia, L. Zhang, W. Zhou and T. Jiao, Surfactant-Assisted Synthesis of Micro/Nano-Structured LiFePO4 Electrode Materials with Improved Electrochemical Performance, *Materials*, 2022, **15**(24), 8953.

36 J. Sun and W. Zhai, Effect of Particle Size on Solubility, Dissolution Rate, and Oral Bioavailability: Evaluation Using Coenzyme Q10 as Naked Nanocrystals, *Inter. J. Nanomed.*, 2012, 5733–5744.

37 Z. Yang, G. Cao, J. Xie and X. Zhao, Oleic Acid-Assisted Preparation of LiMnPO4 and Its Improved Electrochemical Performance by Co Doping, *J. Solid State Electrochem.*, 2012, **16**, 1271–1277.

38 X. Chen, H. Xu, C. Hua, J. Zhao, Y. Li and Y. Song, Synthesis of Silica Microspheres—Inspired by the Formation of Ice Crystals—With High Homogeneous Particle Sizes and Their Applications in Photonic Crystals, *Materials*, 2018, **11**(10), 2017.